RESEARCH ARTICLE
SPACE PHYSICS: MAGNETOSPHERIC PHYSICS

Earth and Planetary Physics
8: 776–786, 2024
doi: 10.26464/epp2024053

Assessing the performance of magnetopause models based on THEMIS data

Yang Lin, JianYong Lu*, BaoHang Qu, and Xi Wang

Institute of Space Weather, School of Atmospheric Physics, Nanjing University of Information Science & Technology, Nanjing 210044, China

Key Points:

- We use a database containing 184,292 magnetopause crossing points.
- Important solar wind parameters associated with Shue98 model errors include the interplanetary magnetic field (IMF) cone angle, IMF B_y, B_z, and dipole tilt.
- The empirical model is compared with a global magnetohydrodynamic simulation model.

Citation: Lin, Y., Lu, J. Y., Qu, B. H., and Wang, X. (2024). Assessing the performance of magnetopause models based on THEMIS data. *Earth Planet. Phys.*, *8*(5), 776–786. http://doi.org/10.26464/epp2024053

Abstract: The magnetopause is the boundary between the Earth's magnetic field and the interplanetary magnetic field (IMF), located where the supersonic solar wind and magnetospheric pressure are in balance. Although empirical models and global magnetohydrodynamic simulations have been used to define the magnetopause, each of these has limitations. In this work, we use 15 years of magnetopause crossing data from the THEMIS (Time History of Events and Macroscale Interactions during Substorms) spacecraft and their corresponding solar wind parameters to investigate under which solar wind conditions these models predict more accurately. We analyze the pattern of large errors in the extensively used magnetopause model and show the specific solar wind parameters, such as components of the IMF, density, velocity, temperature, and others that produce these errors. It is shown that (1) the model error increases notably with increasing solar wind velocity, decreasing proton density, and increasing temperature; (2) when the cone angle becomes smaller or $|B_x|$ is larger, the Shue98 model errors increase, which might be caused by the magnetic reconnection on the dayside magnetopause; (3) when $|B_y|$ is large, the error of the model is large, which may be caused by the east–west asymmetry of the magnetopause due to magnetic reconnection; (4) when B_z is southward, the error of the model is larger; and (5) the error is larger for positive dipole tilt than for negative dipole tilt and increases with an increasing dipole tilt angle. However, the global simulation model by Liu ZQ et al. (2015) shows a substantial improvement in prediction accuracy when IMF B_x, B_y, or the dipole tilt cannot be ignored. This result can help us choose a more accurate model for forecasting the magnetopause under different solar wind conditions.

Keywords: magnetopause; empirical model; global magnetohydrodynamic simulation; THEMIS; solar wind parameters

1. Introduction

The Earth's magnetopause is the boundary between the terrestrial magnetosphere and the solar wind, separating most of the solar wind plasma from the region dominated by the Earth's magnetic field. The outer magnetopause has a weak interplanetary magnetic field (IMF) with a high density and low temperature of solar wind plasma, whereas the inner magnetopause has a strong magnetic field with a low density and high temperature of plasma. The polar cusp regions, located in the northern and southern hemispheres, provide direct access to the magnetosphere for solar wind plasma. The shape of the magnetopause is affected by the solar wind, the Earth's internal magnetic field, and the current system at the same time. The position of the magnetopause is defined by the pressure balance between the solar wind and the magnetosphere, which looks simple but is actually complicated. The pressure on the outside of the magnetopause is mainly dominated by the dynamic pressure from the solar wind plasma and the magnetic pressure from the IMF. Because of the large amount of solar wind plasma intercepted at the magnetopause, the pressure on the inside of the magnetopause is primarily the magnetic pressure of the magnetospheric magnetic field, with a small plasma thermal pressure as well.

The magnetopause is mainly affected by the solar wind dynamic pressure and IMF B_z. When the solar wind dynamic pressure increases, the subsolar distance of the magnetopause decreases (Shue et al., 1997, 1998; Lin RL et al., 2010; Liu ZQ et al., 2015) and the magnetotail flaring angle increases slightly (Shue et al., 1997; Lu JY et al., 2011). For the southward IMF, the magnetopause moves toward the Earth (Aubry et al., 1970), the distance of movement increases with an increase in the southward IMF (Fairfield, 1971), and the magnetotail flaring angle is larger (Formisano et al., 1979). The IMF B_z also affects the subsolar distance and cusp

First author: Y. Lin, 202183300583@nuist.edu.cn
Correspondence to: J. Y. Lu, jylu@nuist.edu.cn
Received 16 JUN 2024; Accepted 19 AUG 2024.
First Published online 10 SEP 2024.

geometry. As the IMF increases in a northward direction, the cusp region moves away from the equatorial plane, and the subsolar magnetopause shifts outward from the Earth (Palmroth et al., 2001).

Apart from the dynamic pressure of the solar wind and IMF B_z, the IMF B_x, B_y, and dipole tilt angle have a nonnegligible influence on the magnetopause (Sibeck et al., 1986; Šafránková et al., 2005; Dušík et al., 2010; Liu ZQ et al., 2015). When the IMF B_y is present, the magnetotail becomes distorted, and a positive (negative) IMF B_y will twist the magnetotail in a counterclockwise (clockwise) direction (Maezawa and Hori, 1998; Liu ZQ et al., 2015). The IMF B_x affects the location of the magnetopause and the cross-section of the magnetotail. A sufficiently large B_x can result in a displacement of the magnetopause location as large as 1.5 R_E (Earth radii). The cross-sectional area of the magnetotail is elongated in a specific direction that closely aligns with the orientation of the IMF (Dušík et al., 2010; Liu ZQ et al., 2015). The IMF cone angle θ_{cone} is the angle between the IMF vector and the Earth–Sun line, which is not included in the model. A quasi-radial (IMF cone angle $\theta_{cone} < 30°$) IMF favors the expansion of magnetopause crossings (MPCs; Fairfield et al., 1990; Dušík et al., 2010; Suvorova et al., 2010; Samsonov et al., 2012; Grygorov et al., 2017; Grimmich et al., 2023). The dipole tilt is an influential factor inside the magnetopause, and as the dipole tilt angle increases positively, the subsolar magnetopause moves below the equatorial plane (Boardsen et al., 2000). The dipole tilt angle influences the cusp locations, the degree of the *z*-axis asymmetry, and the azimuthal asymmetry of the magnetopause (Liu ZQ et al., 2012). The flaring angle increases with increasing dipole tilt in the northern hemisphere, whereas it decreases in the southern hemisphere. In addition, the direction of the dipole tilt angle affects the magnetotail magnetopause, which shifts outward by 4 R_E when the dipole tilt angle changes from negative to positive in the northern hemisphere (Šafránková et al., 2005).

Over the years, various empirical models of the magnetopause have been made (e.g., Petrinec and Russell, 1996; Shue et al., 1997, 1998; Chao JK et al., 2002; Lin RL et al., 2010; Nguyen et al., 2022). These empirical magnetopause models use different observation datasets to determine the magnetopause, typically with the solar wind dynamic pressure and the IMF B_z as input parameters (Petrinec and Russell, 1996; Shue et al., 1997, 1998). Newer models consider the magnetopause asymmetry and polar cusp regions. For example, Lin RL et al. (2010) and Nguyen et al. (2022) used additional parameters, such as the solar wind magnetic pressure and dipole tilt angle. Almost all empirical models assume something a priori about the shape of the magnetopause. For example, the most used model (Shue et al., 1998, hereafter called the Shue98 model) assumes a function of the form

$$r = r_0\left(\frac{2}{1+\cos\theta}\right)^{\alpha}, \tag{1}$$

where r is the radial distance, r_0 is the position of the subsolar point, and θ is the solar zenith angle, respectively. Alpha, α, represents the characteristic of the magnetotail being open or closed, with $\alpha = 0.5$ as the boundary value, whereas $\alpha > 0.5$ indicates an open magnetotail and $\alpha < 0.5$ indicates a closed magnetotail. This assumption might lead to errors in the cusp region, where the magnetopause is closer to the Earth and the geometry has become non-axisymmetric (Boardsen et al., 2000). Since 1998, the Shue98 model has become the most popular model of the magnetopause.

Additionally, the shape and location of the magnetopause can be identified by using the results of global magnetohydrodynamic (MHD) simulations (Elsen and Winglee, 1997; García and Hughes, 2007; Lu JY et al., 2011; Liu ZQ et al., 2015). In contrast to the empirical model, in this approach every point on the magnetopause satisfies the pressure balance condition, and the shape of the magnetopause is non-axisymmetric. In addition, the MHD models can add more input parameters. For example, Liu ZQ et al. (2015) included all IMF components, the solar wind dynamic pressure, and the dipole tilt angle as parameters to achieve higher prediction accuracy under normal solar wind conditions. However, the global MHD models do not appropriately cover all magnetospheric current systems, especially ring currents. As a result, errors also occur in the magnetopause positions obtained from MHD simulations (Samsonov et al., 2016). Liu ZQ et al. (2015) compared their global MHD model with the empirical models of Shue et al. (1998) and Lin RL et al. (2010). For 2849 MPC events, the distribution of the standard deviation of the three models in different regions showed that their simulations were even better than the well-established empirical models. Gordeev et al. (2015) compared the results of the MHD simulations with the empirical model of Shue et al. (1998) at the subsolar point and the empirical model of Lin RL et al. (2010) at high latitudes, and concluded that the MHD predictions correlated well with the empirical model results. Samsonov et al. (2016) made similar comparisons but examined the influence of the ring current magnetic field.

However, many factors can affect the performance of the above-mentioned models. Especially under extreme conditions, most models are unable to predict the exact magnetopause position well (Tátrallyay et al., 2012; Suvorova and Dmitriev, 2015). Grimmich et al. (2023) used 184,292 observed MPCs to assess the performance of the typical empirical magnetopause model by Shue et al. (1998) and found that the magnetopause expanded or compressed under some solar wind conditions. Regrettably, they did not provide the main solar wind factors driving extreme events.

In this study, we focus on the location of the extreme MPCs. We identify the parameters that are most likely to affect the accuracy of the Shue98 model and select appropriate models for different solar wind conditions. We use a 15-year database of MPCs to statistically study extreme magnetopause positions and make performance comparisons between empirical and simulation models. This paper is organized as follows: Section 2 describes the spacecraft data and the databases we use, Section 3 shows the prediction error analysis of the magnetopause model and compares the prediction effects of two typical magnetopause models, Section 4 discusses our results, and Section 5 summarizes our findings.

2. Data and Methods

The spacecraft of the THEMIS (Time History of Events and Macroscale Interactions during Substorms) mission have been launched into Earth's orbit since 2007 to operate and probe electromagnetic data in near-Earth space (Angelopoulos, 2008). Using magnetic field data from the Fluxgate Magnetometer (Auster et al., 2008) and data on the moments and particle fluxes from the Electrostatic Analyzer (McFadden et al., 2008), Grimmich et al. (2023) identified the MPCs from 2007 to 2022. During these 15 years, the THEMIS spacecraft observed a total of 184,292 MPCs. These data are mainly from probes TH-A, TH-D, and TH-E. The TH-B and TH-C probes were redirected to the lunar orbit in 2010 for use in the ARTEMIS (Acceleration, Reconnection, Turbulence and Electrodynamics of Moon's Interaction with the Sun) mission (Angelopoulos, 2011), so their data are available only through the end of 2009. These MPCs are collected in the dataset TH-MPC (Grimmich et al., 2023). During construction of the TH-MPC database, Grimmich et al. (2023) used a machine learning approach in the MPC identification process and a random forest classifier to infer crossing events from the automatically labeled data. This method improves the accuracy of the identification, although some misidentifications still occur. The Low Latitude Boundary Layer contains a mixture of magnetosheath and magnetospheric plasma, which makes a clear separation of these two regions difficult. This confusion leads to multiple events being recognized as a single MPC. In addition, in the high-longitude region near the terminator, Kelvin–Helmholtz instability-induced plasma mixing makes it difficult for MPCs to be clearly identified. Magnetopause crossings with low crossing probabilities are also included in the database. These misidentifications may affect the statistical features extracted from the database, such as the mean position of the MPC, the standard deviation, and the correlation analysis with solar wind parameters.

We create a database based on the TH-MPC dataset, which contains the locations of the MPCs, the corresponding solar wind parameters, and radial distances from the magnetopause models of Shue et al. (1998) and Liu ZQ et al. (2015; hereafter called as Liu15). The solar wind parameters are obtained from the high-resolution 1-min OMNI dataset, where the dipole tilt angles are calculated from the time data in the OMNI dataset. The MPC position data contain the orbital dataset of the THEMIS probe in Geocentric Solar Magnetospheric (GSM) coordinates (*X*, *Y*, *Z*) and spherical coordinates with a 1-min resolution. The modeling equations of the Shue98 model are as follows:

$$r = r_0\left(\frac{2}{1+\cos\theta}\right)^{\alpha}, \tag{2}$$

$$r_0 = \left\{10.22 + 1.29\tanh\left[0.184\left(B_z + 8.14\right)\right]\right\}P_d^{-\frac{1}{6.6}}, \tag{3}$$

$$\alpha = \left(0.58 - 0.007B_z\right)\left(1 + 0.024\ln P_d\right). \tag{4}$$

In addition, the modeling equations of the Liu15 model are as follows:

$$r = r_0\left(\frac{2}{1+\cos\theta}\right)^{\alpha}\left(1 - 0.1C\cos^2\varphi\right), \tag{5}$$

$$\alpha = \alpha_0 + \left[\alpha_\phi + \delta_\alpha \mathrm{sgn}\left(\cos\varphi\right)\right]\cos\left[2\left(\varphi - \omega\right)\right] + \alpha_z\cos\varphi, \tag{6}$$

$$C = \exp\left(-\frac{|\theta - l_n|}{W_n}\right)\left[\mathrm{sgn}\left(\cos\varphi\right) + 1\right] + \exp\left(-\frac{|\theta - l_s|}{W_s}\right)\left[\mathrm{sgn}\left(-\cos\varphi\right) + 1\right], \tag{7}$$

$$r_0 = \left\{10.56 + 0.956\tanh\left[0.1795\left(B_z + 10.78\right)\right]\right\}\left(P_d + P_m\right)^{-0.1699}, \tag{8}$$

$$\begin{cases} l_n = \left\{0.822 + 0.2921\tanh\left[0.08792\left(B_z + 10.12\right)\right]\right\}\left(1 - 0.01278\psi\right) \\ l_s = \left\{0.822 + 0.2921\tanh\left[0.08792\left(B_z + 10.12\right)\right]\right\}\left(1 + 0.01278\psi\right) \end{cases}, \tag{9}$$

$$\begin{cases} W_n = \left(0.2382 + 0.005806\log P_d\right)\left(1 + 0.0002335\psi^2\right) \\ W_s = \left(0.2382 + 0.005806\log P_d\right)\left(1 + 0.0002335\psi^2\right) \end{cases}, \tag{10}$$

$$\alpha_0 = \left\{0.4935 - 0.1095\tanh\left[0.1091\left(B_z - 6.882\right)\right]\right\}\left(1 + 0.01182\log P_d\right), \tag{11}$$

$$\alpha_\phi = \left\{0.06354 - 0.07764\tanh\left[0.07217\left(|B_z| - 4.851\right)\right]\right\}\left(1 - 0.1331\log P_d\right), \tag{12}$$

$$\delta_\alpha = 0.02582\tanh\left(0.0667B_x\right)\mathrm{sgn}\left(B_z\right), \tag{13}$$

$$\omega = \tan^{-1}\left[0.1718\left(B_y/B_z\right)\sqrt{B_y^2 + B_z^2}^{\,0.387}\right], \tag{14}$$

$$\alpha_Z = 0.06263\tanh\left(0.0251\psi\right), \tag{15}$$

where φ is the azimuthal angle (starting from the direction of the positive *z*-axis), ψ is the dipole tilt angle, l_n/l_s and W_n/W_s are the position and width of the pole-tip region (north/south), and α_0 denotes the degree of flaring of the magnetic tail.

We apply statistical methods to study the quantitative distribution of the solar wind parameters. At the same time, we calculate the radial distances of the Shue98 model and the Liu15 model as well as the deviation of the radial distances of each MPC. Similar to Grimmich et al. (2023), we classify the MPCs with absolute deviation exceeding 1.5 R_E as large errors of the model and those lower than 1.5 R_E as small errors of the model. We then investigate the specific location of the modeling error and the solar wind parameters causing the model error.

3. Results

3.1 Error Analyses of Shue98

In this section, we statistically characterize the error spatial distribution of the Shue98 model and the corresponding solar wind conditions. In addition, the characteristics of the error distribution of the Shue98 model and its relationship with the solar wind conditions are analyzed.

Figure 1 illustrates the spatial distribution of errors, calculated from the Shue98 model result minus the corresponding observed MPC location for MPCs, as well as the spatial distribution of errors with absolute values exceeding 1.5 R_E. Each point represents an MPC, and the color indicates the size of the error. As shown in Figures 1a, 1b, and 1c, the MPCs are mainly located in the low latitudes on the dayside. The Shue98 model shows a notable underestimation around the outer edge of the sunward side at low latitudes, whereas it shows a notable overestimation on the inner side of the dawn–dusk sides. To highlight the spatial distribution of large errors in the Shue98 model, we count the distribution of MPCs with errors exceeding 1.5 R_E, as shown in Figures 1d, 1e, and 1f. From the spatial distribution of large errors, it can be seen that the Shue98 model as a whole underestimates the MPCs when

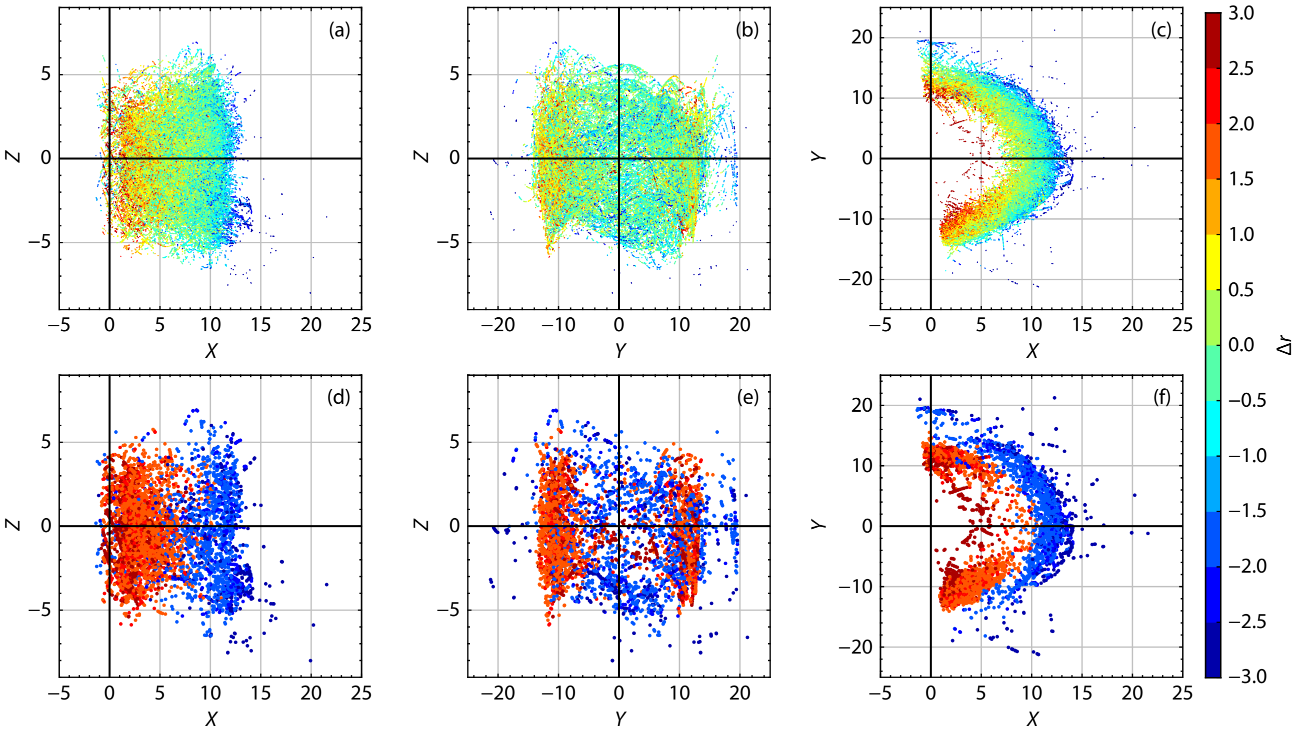

Figure 1. In the GSM coordinate system, the spatial distribution of errors (the Shue98 model results minus observations) at all MPC point positions, as well as the spatial distribution of errors with absolute values exceeding 1.5 R_E. The projections from left to right are in the *X*–*Z* plane, *Y*–*Z* plane, and *X*–*Y* plane, respectively. Each point represents one MPC, and the color indicates the size of the error. A positive error indicates overestimation of the Shue98 model, whereas a negative error indicates underestimation of the Shue98 model.

$X_{GSM} > 7\ R_E$ but makes an overestimation for $X_{GSM} < 7\ R_E$.

To analyze the sources of errors in the Shue98 model, we separately count the amount of data for all MPCs and the distributions of the two subsets of the Shue98 model, the large and small errors, with the variation of the solar wind parameters, as shown in Figure 2. Note that these statistics are normalized. In addition, the solar wind parameters mainly include the three components of the IMF and the cone angle (θ_{cone}), clock angle (θ_{clock}), flow speed (v), proton density (n), temperature (t), dynamic pressure (P_d), plasma β value (β), Alfven Mach number (M_A), and dipole tilt angle (ψ). The black lines show the distribution of solar wind data for all MPCs, and the blue and purple lines show the distribution of the large and small errors, respectively. The maximum and median values of the statistical parameters are shown in the corresponding colors.

As shown in Figure 2, the solar wind parameters of most MPCs are mainly centered around typical solar wind conditions, such as $|B_x| < 4$ nT, $|B_y| < 4$ nT, $|B_z| < 3$ nT, and so on. However, relatively few MPCs are under extreme solar wind conditions. Furthermore, Figure 2 shows that the distribution of solar wind conditions for the two types of errors is very similar to the distribution of solar wind conditions for all MPCs. The reason for this phenomenon is that regardless of whether the errors are large or small, the crossing point data are always concentrated near typical solar wind conditions, whereas fewer data are available under extreme solar wind conditions. As a result, we are unable to identify the parameters affecting model accuracy, nor can we determine the range of parameters within which the Shue98 model predictions are inaccurate. Comparing the maximum and median solar wind conditions for the three cases (large errors, small errors, and all data) reveals some shifts in the large and small errors, with the shift in the large errors being slightly more obvious. For example, in Figures 2d, 2e, 2f, and 2k, the large error data have a large dynamic pressure bias, a large solar wind speed bias, a small proton density bias, and a small cone angle bias.

To eliminate the effect of data inhomogeneity, we separately calculate the percentage of large and small errors in different solar wind parameter intervals for the Shue98 model. In addition, to avoid the fact that the amount of data in some extreme solar wind conditions is too small to affect the statistical results, we exclude the part of each parameter that accounts for less than 2%. In Figure 3, the *Y*-axis presents the two types of errors as a function of a specific solar wind condition. The probability of notable errors is shown as orange lines, and the probability of small errors as blue lines, respectively. We mainly focus on the orange lines in Figure 3. In Figure 3a, the probability of notable errors of the Shue98 model increases markedly as $|B_x|$ increases. The error is most noticeable for $-5\ \text{nT} < B_x < -3$ nT. In Figure 3b, at $|B_y| < 4$ nT, the error of the Shue98 model shows a tendency to diminish as $|B_y|$ increases, whereas the error is most pronounced at the $|B_y|$ extremes and $-2\ \text{nT} < B_y < 2$ nT. In Figure 3c, the error in the Shue98 model is larger when B_z is southward. Figures 3e, 3f, and 3g show that the model error increases markedly with increasing solar wind velocity, decreasing proton density, and increasing temperature. Figure 3j points out that the error is larger when the dipole tilt angle is positive than when it is negative and that it

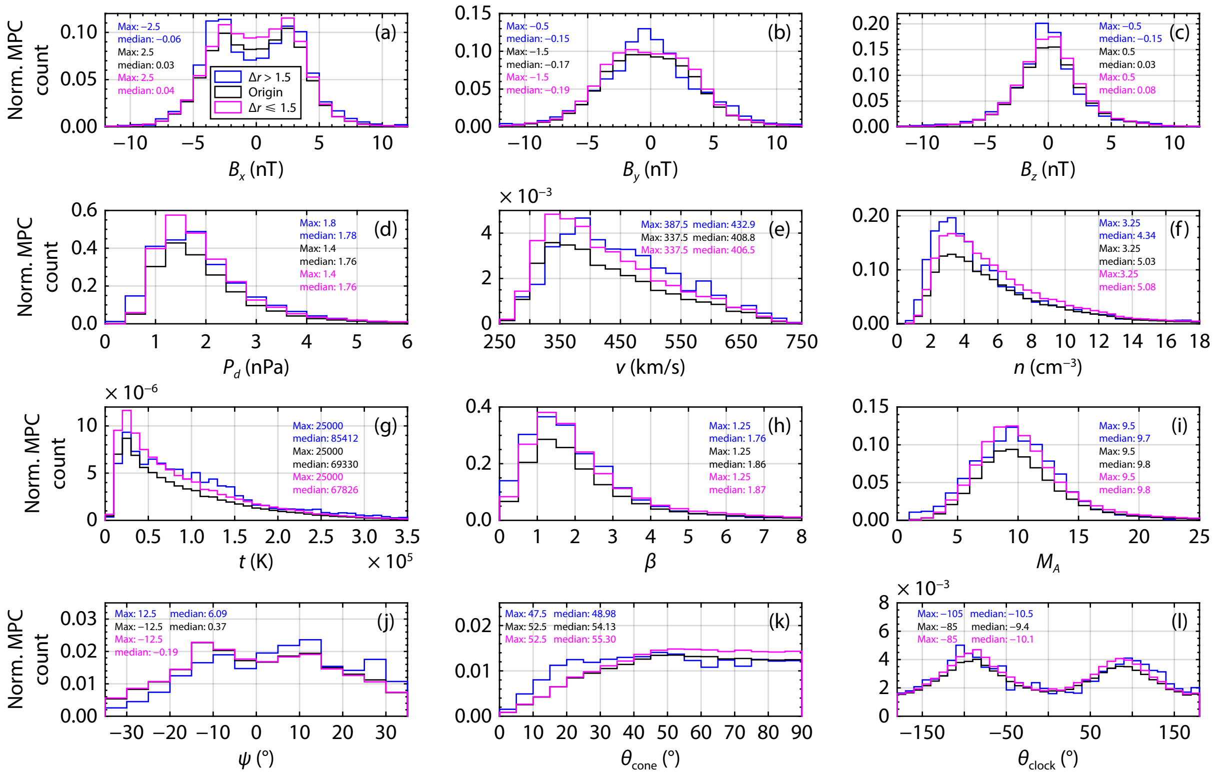

Figure 2. Normalized distributions of large errors, small errors, and the amount of all MPC data as a function of the variation of individual solar wind parameters. These solar wind parameters include the three components of the IMF and the dynamic pressure (P_d), flow speed (v), proton density (n), temperature (t), plasma β value (β), Alfven Mach number (M_A), dipole tilt angle (ψ), cone angle ($\theta_{\rm cone}$), and clock angle ($\theta_{\rm clock}$). The blue color denotes errors larger than 1.5 $R_{\rm E}$, the purple color denotes errors smaller than 1.5 $R_{\rm E}$, and the black color denotes the data volume for all the data at the MPC. The maximum and median values for each case are labeled in each panel with the corresponding color.

increases with increasing dipole tilt angle. In Figure 3k, the error of the model decreases as the cone angle increases, and it is most evident at the cone angle from 10° to 30°.

To investigate the specific effects of the above-mentioned parameters on the Shue98 model, we focus on the regions with large errors in the Shue98 model and specifically analyze the effects of each parameter on the location. Because the errors of the Shue98 model mainly consist of underestimation at $X_{\rm GSM} > 7\ R_{\rm E}$ and overestimation at $X_{\rm GSM} < 7\ R_{\rm E}$ (hereafter called two large error source regions), when analyzing the distribution of each parameter in these regions where the Shue98 model prediction results have large errors, we show only the results in the X–Y plane for the parameters except dipole tilt angle, as shown in Figure 4. The results of the dipole tilt angle are presented on three projection surfaces, X–Z, Y–Z, and X–Y, as shown in Figure 5.

In Figures 4a and 4b, it can be seen that the larger $|B_x|$ and smaller cone angle are distributed in both the $X_{\rm GSM} > 7\ R_{\rm E}$ and $X_{\rm GSM} < 7\ R_{\rm E}$ regions. These two conditions lead to increased inaccuracy in the Shue98 model predictions, which explains why two large error source regions of the Shue98 model are affected by $|B_x|$, with the effect being more pronounced near the subsolar sectors. The spatial distribution of $|B_y|$ (see Figure 4c) shows that, in the extreme cases, the errors caused by $|B_y|$ are mainly found at $X_{\rm GSM} < 7\ R_{\rm E}$, whereas at -2 nT $< B_y <$ 2 nT, two large error source regions can occur, especially at $X_{\rm GSM} > 7\ R_{\rm E}$. The corresponding B_z values for the MPCs in the large error source regions (see Figure 4d) suggest that when B_z is close to 0, the large error source region is mainly concentrated at $X_{\rm GSM} > 7\ R_{\rm E}$. Compared with B_z close to 0, the errors in $B_z < 0$ are less. In contrast, at $X_{\rm GSM} < 7\ R_{\rm E}$, B_z is predominantly negative or close to 0. The spatial distribution of solar wind velocity and proton density (see Figures 4e and 4f) indicates that at higher velocity and lower density, two large error source regions can occur, especially at $X_{\rm GSM} > 7\ R_{\rm E}$. In the spatial distribution of temperature (see Figure 4g), although some MPCs in the two large error source regions correspond to higher temperature conditions, as shown in Figure 2g, the number of MPCs with lower temperatures is much higher. Therefore, the MPCs with lower temperatures in Figure 4g are also more widely distributed in the two large error source regions. The positive dipole tilt angle in Figure 5 is distributed in the fourth quadrant of the Y–Z plane, whereas the negative dipole tilt angle is distributed in the second quadrant of the Y–Z plane, which is consistent with the findings of Boardsen et al. (2000).

3.2 Model Comparisons

As mentioned above, the Shue98 model predicts increased errors under extreme conditions for parameters such as IMF B_x, B_y, and the dipole tilt angle. For this reason, we are interested in examining the performance of the Liu15 model compared with the Shue98 model. The Liu15 model is based on MHD model simulations and has three more input parameters than the Shue98 model, including

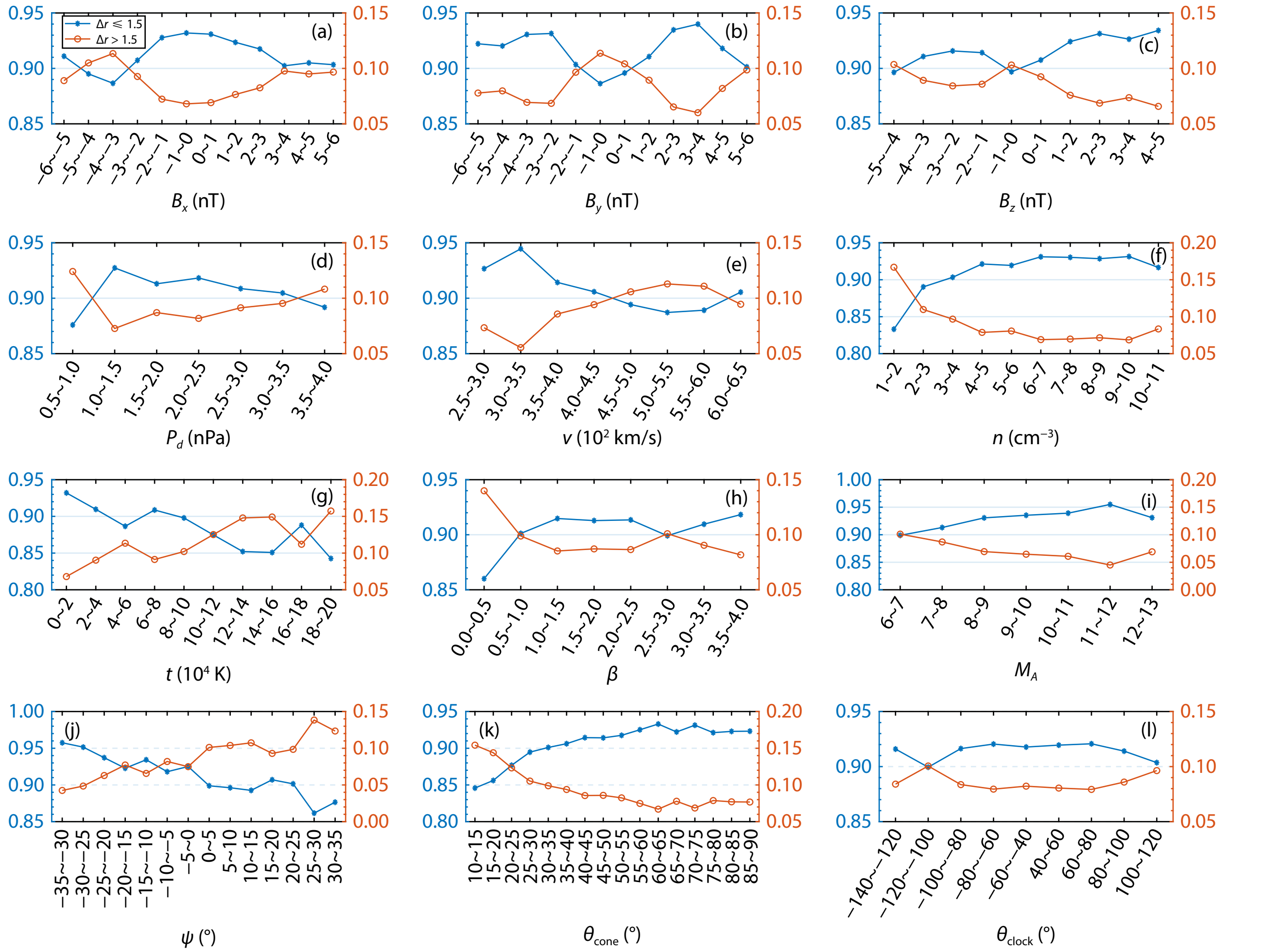

Figure 3. Large and small error trends of the Shue98 model as a proportion of the different solar wind parameter segments, with the blue line representing the probability of the small error trend corresponding to the blue *Y*-axis on the left, and the orange line representing the probability of the notable error trend corresponding to the orange *Y*-axis on the right.

IMF B_x, B_y, and the dipole tilt angle. We compare and analyze the advantages of the two models under different solar wind conditions and over different areas.

Figure 6 for all the MPC data shows the error statistics of the Liu15 model and the Shue98 model over various X_{GSM} ranges. The lines at the bottom, top, and center of each box represent, respectively, the upper quartile, lower quartile, and median of the sample. The dashed lines reflect the range of error, with the highest points representing the maximum errors and the lowest points representing the minimum errors. The blue box-line plots display the statistics for Shue98, and the orange box-line plots display the statistics for Liu15. When $X_{GSM} > 12$ R_E or $X_{GSM} < -1$ R_E, the two models behave unstably and predict inaccurately, especially near the subsolar sectors. When comparing the error statistics of the two models, we find that the Shue98 model has a larger error at $X_{GSM} < 7$ R_E, whereas the error values of the two models are relatively close to each other at $X_{GSM} > 7$ R_E, and that the Shue98 model has slightly smaller errors.

To further analyze the advantages and disadvantages of the two models, we conduct an error analysis of the Liu15 model on the MPC data in large error source regions of Shue98, as shown in Figure 7. When comparing Figures 1d, 1e, and 1f, we can see that small error points are evident mainly at $X_{GSM} < 7$ R_E, indicating that the optimization of the Liu15 model occurs mainly at $X_{GSM} < 7$ R_E, with no apparent improvement at $X_{GSM} > 7$ R_E, which is similar to the statistics for the full data above.

As mentioned in the previous section, the effect of solar wind conditions on the Shue98 model error is remarkable, especially for IMF B_x, B_y, B_z, and the dipole tilt angle. The Shue98 model itself does not include the effects of IMF B_x, B_y, and the dipole tilt angle, whereas the Liu15 model includes the effects of these parameters. Therefore, we statistically analyze the variation of the Liu15 model error with IMF B_x, B_y, and the dipole tilt angle, and compare the results with the Shue98 model. Figure 8 demonstrates the percentage of large and small errors with the cone angle, B_y, and dipole tilt angle for the Liu15 model. Note that Figure 8 uses the same statistical method as Figure 3. We compare Figure 8a with Figure 3k, Figure 8b with Figure 3b, and Figure 8c with Figure 3j, respectively. We find that the frequency of small error points in cone angle sections is generally greater than 95% for Liu15, whereas the frequency of small error points is generally less than 95% for Shue98. In contrast, the Liu15 model is better than the Shue98 model in the trend of error percentage, and the Liu15

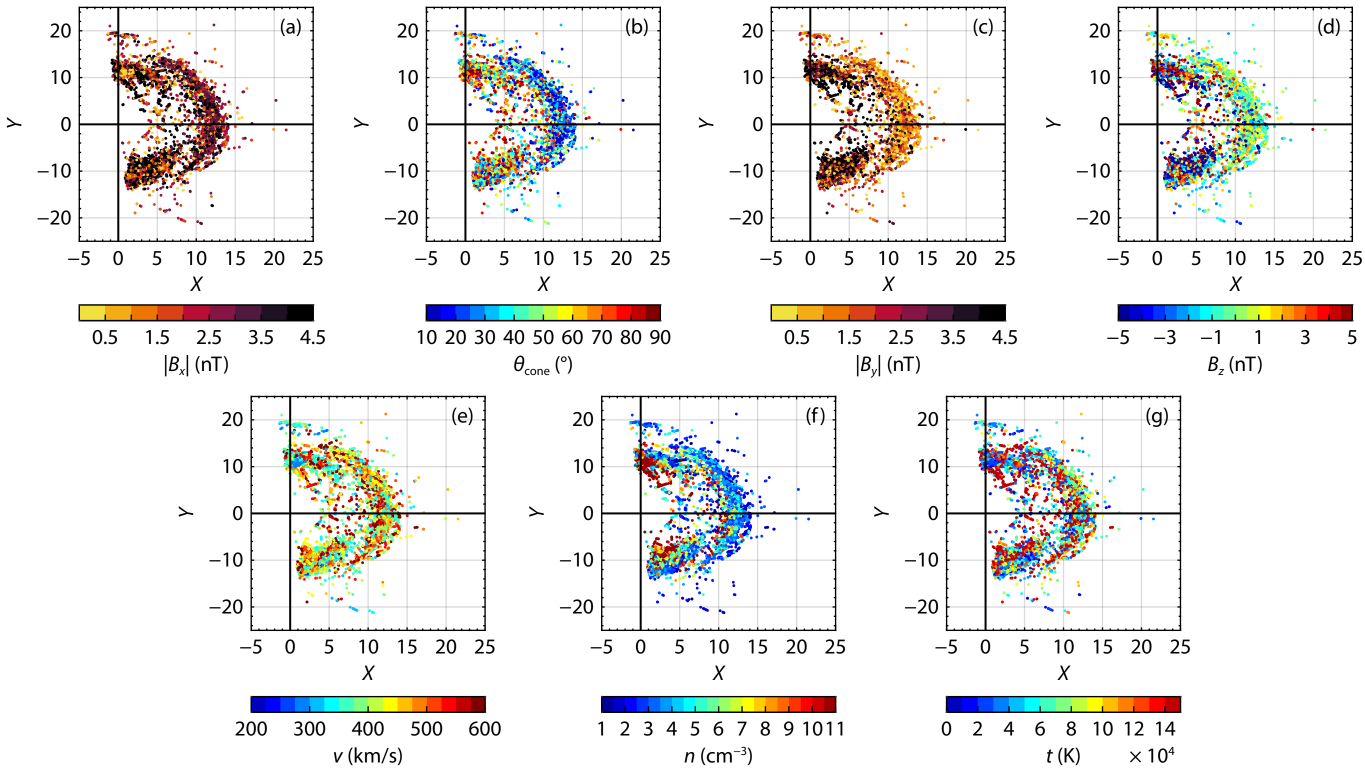

Figure 4. In the GSM coordinate system, the distribution of MPCs in the X–Y plane for Shue98 errors exceeding 1.5 R_E. Each point represents an MPC, and the colors indicate the size of the different parameters. These solar wind parameters include IMF $|B_x|$, $|B_y|$, B_z, θ_{cone}, v, n, and t.

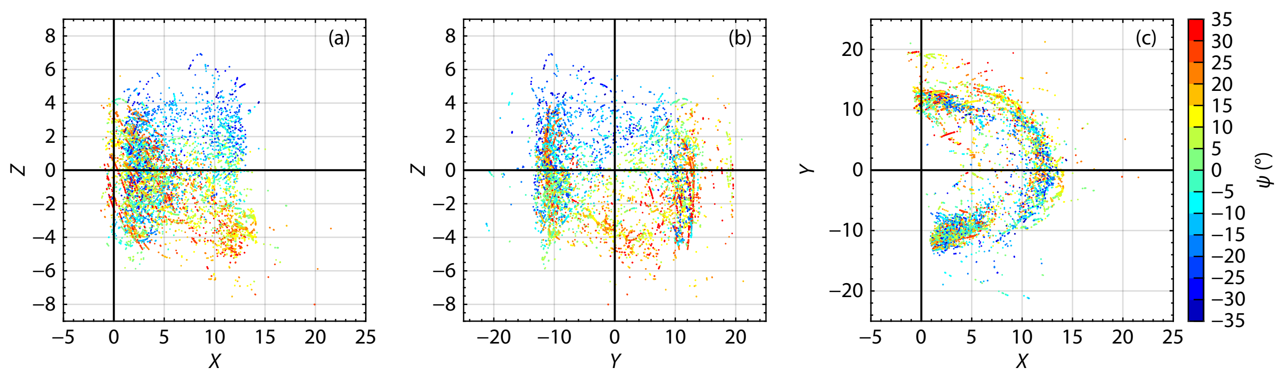

Figure 5. In the GSM coordinate system, the distribution of MPCs with the Shue98 model errors exceeding 1.5 R_E. Each point represents an MPC, and the colors indicate the size of the dipole tilt angle, from left to right, the projections in the X–Z plane, the Y–Z plane, and the X–Y plane.

model has very outstanding performance when the cone angle is small. The frequency of small error points in IMF B_y for the Liu15 model is greater than 90%, and most are greater than 95%. Although the Liu15 model still presents the trend that the error of the model increases in the extreme case of IMF B_y, the Liu15 model describes the MPC better than the Shue98 model. Moreover, the accuracy is somewhat improved in the zones of the dipole tilt angle.

4. Discussion

In this section, we discuss the effects of different solar wind parameters on the errors of the Shue98 model and analyze the corresponding sources and causes of the errors. In addition, we discuss the advantages and characteristics of the Liu15 model and the Shue98 model.

The MPCs of THEMIS are mostly located in the low-latitude region on the dayside. According to the results of the Shue98 model, large model prediction errors occur at the periphery of the sunward side at low latitudes and the inner part of the dawn–dusk sides, which is at $X_{GSM} > 7\ R_E$ and $X_{GSM} < 7\ R_E$. These phenomena may not be completely explained by the input parameters of the Shue98 model (e.g., variations in solar wind dynamic pressure P_d or IMF B_z) but may be related to other solar wind conditions. By quantifying the effects of different solar wind parameters on the model prediction errors, we can infer several solar wind parameters and their parameter ranges that have a substantial effect on the magnetopause position. In the large error regions, the parameter values corresponding to the MPCs reveal the specific effects of the various parameters on the prediction inaccuracy for the Shue98 model.

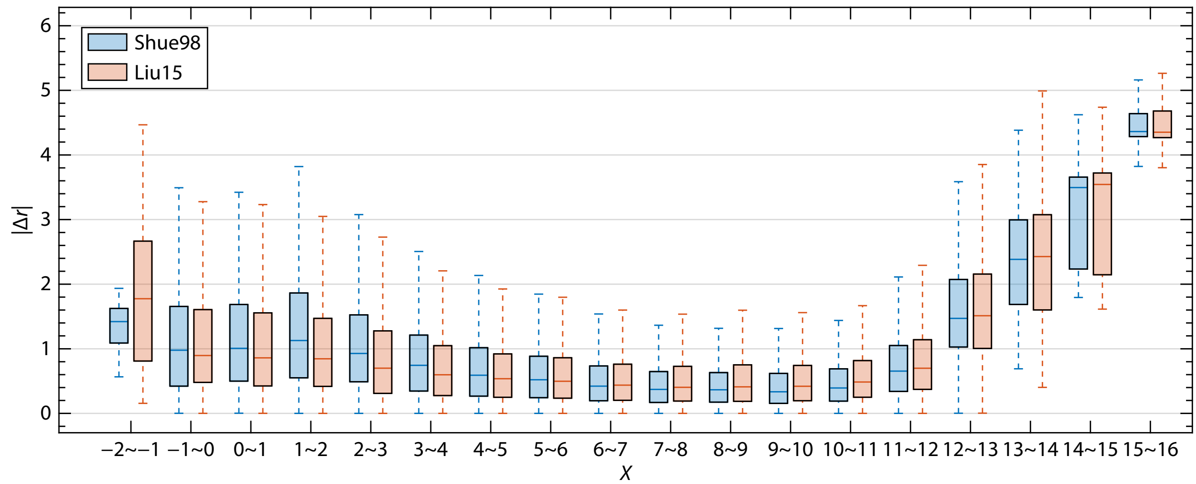

Figure 6. A statistical figure of the Liu15 model (orange) and the Shue98 model (blue) with the errors of all the MPCs at different locations. The lines at the bottom, top, and center of each box indicate, respectively, the upper quartile, lower quartile, and median of the sample. The dashed lines extend from the top of each box upward and the bottom downward to the farthest sample values (maximum and minimum).

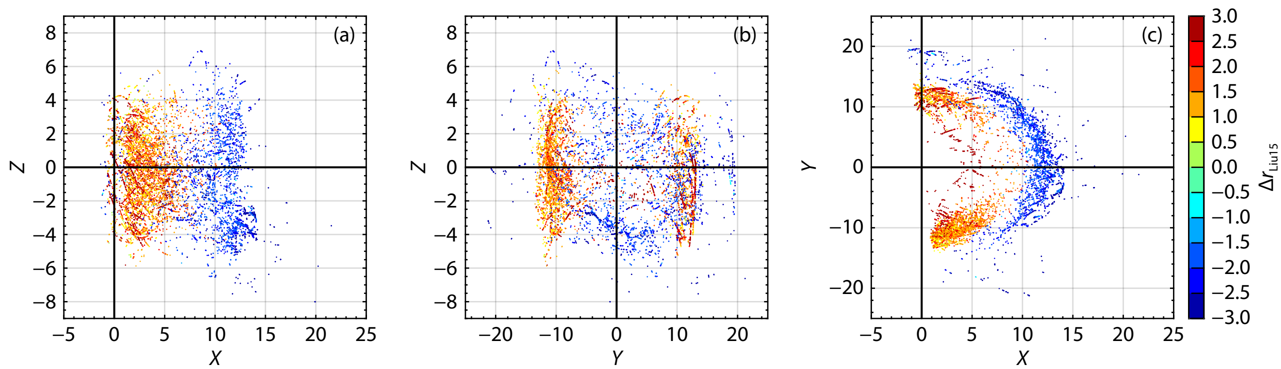

Figure 7. In the GSM coordinate system, the spatial distribution of errors for the Shue98 model and the MPC distribution of errors exceeding 1.5 R_E, where from left to right are the projections in the X–Z plane, the Y–Z plane, and the X–Y plane. Each point represents an MPC, and the color indicates the size of the Liu15 error.

From Figure 3, it is clear that the errors of the Shue98 model are closely related to the three components of the IMF and the cone angle. As $|B_x|$ increases, the large errors of the Shue98 model increase markedly, with both the $X_{GSM} > 7$ R_E and $X_{GSM} < 7$ R_E regions responding to $|B_x|$. The response near the subsolar sectors is more outstanding. The reason for this phenomenon might be the reconnection on the dayside of the magnetopause or the Shue98 model itself, which is not responsive to B_x, or both. Similar to B_x is the effect of the cone angle, which is most evident for the Shue98 model at 10° to 30° and is mostly distributed at $X_{GSM} >$ 7 R_E. Under radial or quasi-radial ($\theta_{cone} \le 30°$) IMF conditions, a quasi-parallel foreshock established in the subsolar region results in the location of the dayside bow shock closer to the Earth, the magnetosheath thickness reduces, and the dayside magnetopause moves sunward (Grimmich et al., 2023), causing an underestimation of the Shue98 model at $X_{GSM} > 7$ R_E.

By analyzing the effects of B_y and B_z with the Shue98 model errors, we find that in the extreme cases of B_y and B_z, the model errors are larger and mainly concentrated in $X_{GSM} < 7$ R_E. The reason for this might be that the larger $|B_y|$ affects the location of the reconnection, which leads to east–west asymmetry of the magnetopause, and then generates errors. However, it is worth noting that the Shue98 model also has notable errors when −2 nT < B_y < 2 nT and B_z is close to 0, and the errors are mainly concentrated at $X_{GSM} >$ 7 R_E. Then, at $X_{GSM} > 7$ R_E, there are in addition very marked effects of B_x and the cone angle. This result suggests that the errors at −2 nT < B_y < 2 nT and B_z approaching 0 are mainly the effects of B_x rather than B_y and B_z. Therefore, B_y and B_z mainly control the errors at $X_{GSM} < 7$ R_E. This might be caused by the southward IMF reconnection driving the magnetopause inward, resulting in an overestimation of the Shue98 model, or it might be the result of the B_x reconnection and B_y working together.

A smaller proton density and larger solar wind speed also cause errors in the Shue98 model and act primarily at $X_{GSM} > 7$ R_E. The sparse plasma leads to decreased dynamic pressure, whereas the high-speed solar wind leads to increased dynamic pressure (Grimmich et al., 2023). In the $X_{GSM} > 7$ R_E region, these two effects cancel each other out. Therefore, the real reasons for the errors should be the B_x or cone angle. The high temperature affects the errors in the $X_{GSM} > 7$ R_E and $X_{GSM} < 7$ R_E regions, whereas the number of MPCs observed in this condition is very low. The increased temperature results in increased thermal pressure, lead-

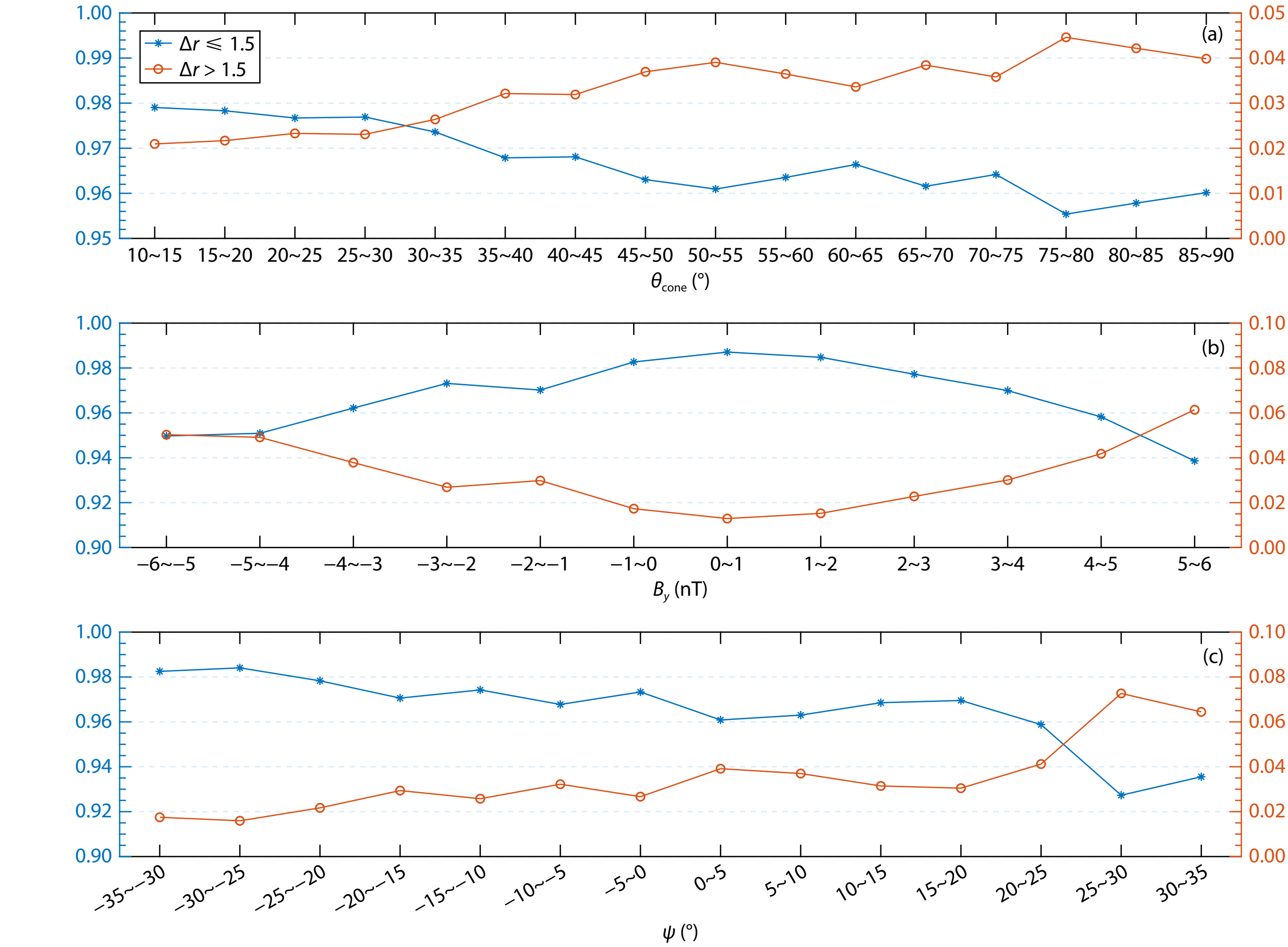

Figure 8. The percentage trends of large and small errors for the Liu15 model in the cone angle, B_y, and dipole tilt angle sections. The blue line represents the small error trend corresponding to the blue Y-axis on the left, and the orange line represents the large error trend corresponding to the orange Y-axis on the right.

ing to a deviation in the position of MPCs.

As shown in Figure 5, there is a clear partitioning of the positive and negative dipole tilt angles, indicating that the dipole tilt angle affects the magnetopause differently in the northern and southern hemispheres. Liu ZQ et al. (2012) showed that the dipole tilt angle does not affect the equatorial magnetopause and mainly affects the south–north asymmetry and rotational asymmetry as well as the cusp geometry of the magnetopause. With a positively increasing dipole tilt angle, the northern cusp moves toward the equatorial plane and the southern cusp moves away from the equatorial plane (Liu ZQ et al., 2015). In addition, the distance below the equatorial plane to the magnetopause increases, which leads to errors. In contrast, the negative dipole tilt angle acts oppositely, causing the error above the equatorial plane to increase.

For model comparison, we chose the Liu15 model to compare with the Shue98 model, and both models were unstable in predicting near the subsolar region. Both the statistical results for all the data and the Liu15 model error values for the MPCs in the large error source regions of the Shue98 model show that the Liu15 model performs better than the Shue98 model at X_{GSM} < 7 R_E, but with no substantial improvement at X_{GSM} > 7 R_E. Regarding the influence of parameters, the errors of the Liu15 model caused by the cone angle, B_y, and dipole tilt angle are all reduced to some degree. This effect is especially noticeable when the cone angle and $|B_y|$ are small, with the percentage of small error points for the Liu15 model exceeding 97% for all of them.

5. Conclusion

In this study, we build a database based on 184,292 MPCs observed by the THEMIS spacecraft from 2007 to 2022 in the TH-MPC dataset and explore the effects of solar wind parameters on the prediction accuracy of the Shue98 model, as well as the corresponding sources and causes of errors. Our statistical results show that B_x, B_y, B_z, the cone angle, and the dipole tilt angle are the main factors affecting the forecast accuracy of the Shue98 model. Through normalization and statistical analysis, the study reveals some trends in the variation of Shue98 model errors with solar wind parameters. The model error increases as $|B_x|$ increases and the cone angle decreases. The model errors are biased large when $|B_y|$ is large, and the model errors increase when B_z is southward. In addition, an increasing solar wind speed, decreasing density, and increasing temperature lead to an increase in the Shue98 model error. A positive dipole tilt angle condition shows larger errors than negative ones and increases with an increase in the dipole tilt angle. Further analysis shows that the errors in the Shue98 model originate mainly from the X_{GSM} > 7 R_E and X_{GSM} < 7 R_E. The spatial distribution of the individual parameters states that (1) the large Shue98 model errors for large $|B_x|$ and small cone angle conditions might be due to magnetic reconnection on the dayside of the magnetopause or the weak response of the model to B_x; (2) the errors for extreme B_y conditions might be caused by east–west asymmetry at the magnetopause caused by magnetic reconnection; (3) the errors induced by B_z might be the result of southward IMF reconnection; and (4) the error is larger for positive dipole tilt than for negative dipole tilt and increases with an increasing dipole tilt angle. In addition, high velocity and low density will affect the two large error source regions; however, the effects cancel each other out and the real cause of the error is B_x, the cone angle, or both.

It is worth mentioning that the values of each parameter are higher at X_{GSM} < 7 R_E, which suggests that the errors in this region are probably the consequence of the influence of more than one factor. In contrast, at X_{GSM} > 7 R_E, $|B_x|$ is larger, the cone angle is smaller, B_y and B_z are weaker, and the velocity is larger while the density is smaller. This indicates that the main influence in this region is B_x. In comparison, the Liu15 model shows a certain improvement in prediction accuracy, especially for smaller cone angles and smaller $|B_y|$. In terms of the dipole tilt angle, the Liu15 model also shows enhanced accuracy. However, the improvement of the Liu15 model mainly occurs at X_{GSM} < 7 R_E, and no substantial improvement occurs at X_{GSM} > 7 R_E.

The exact processes by which the temperature affects the magnetopause are still unclear. In this study, we have included only observations of the low-latitude magnetopause on the dayside. The performance of the proposed magnetopause models at high latitudes and in magnetotail regions still need to be assessed, which we plan to continue to do in the future.

Data Availability Statement

The TH-MPC dataset on which the study is based was accessed from a repository and can be downloaded from the website https://osf.io/b6kux/#!.

Acknowledgments

This work was supported by the National Natural Science Foundation of China (Grant Nos. 42030203, 42004132, 42074195, and 42074183).

References

Angelopoulos, V. (2008). The THEMIS mission. *Space Sci. Rev.*, *141*(1), 5–34. https://doi.org/10.1007/s11214-008-9336-1

Angelopoulos, V. (2011). The ARTEMIS mission. *Space Sci. Rev.*, *165*(1), 3–25. https://doi.org/10.1007/s11214-010-9687-2

Aubry, M. P., Bitoun, J., and Graff, P. (1970). Propagation and group velocity in a warm magnetoplasma. *Radio Sci.*, *5*(3), 635–645. https://doi.org/10.1029/RS005i003p00635

Auster, H. U., Glassmeier, K. H., Magnes, W., Aydogar, O., Baumjohann, W., Constantinescu, D., Fischer, D., Fornacon, K. H., Georgescu, E., … Wiedemann, M. (2008). The THEMIS fluxgate magnetometer. *Space Sci. Rev.*, *141*(1), 235–264. https://doi.org/10.1007/s11214-008-9365-9

Boardsen, S. A., Eastman, T. E., Sotirelis, T., and Green, J. L. (2000). An empirical model of the high-latitude magnetopause. *J. Geophys. Res.: Space Phys.*, *105*(A10), 23193–23219. https://doi.org/10.1029/1998JA000143

Chao, J. K., Wu, D. J., Lin, C. H., Yang, Y. H., Wang, X. Y., Kessel, M., Chen, S. H., and Lepping, R. P. (2002). Models for the size and shape of the Earth's magnetopause and bow shock. *COSPAR Colloq. Ser.*, *12*, 127–135. https://doi.org/10.1016/S0964-2749(02)80212-8

Dušík, Š., Granko, G., Šafránková, J., Němeček, Z., and Jelínek, K. (2010). IMF cone angle control of the magnetopause location: Statistical study. *Geophys. Res. Lett.*, *37*(19), L19103. https://doi.org/10.1029/2010GL044965

Elsen, R. K., and Winglee, R. M. (1997). The average shape of the Magnetopause: A comparison of three-dimensional global MHD and empirical models. *J. Geophys. Res.: Space Phys.*, *102*(A3), 4799–4819. https://doi.org/10.1029/96JA03518

Fairfield, D. H. (1971). Average and unusual locations of the Earth's magnetopause and bow shock. *J. Geophys. Res.*, *76*(28), 6700–6716. https://doi.org/10.1029/JA076i028p06700

Fairfield, D. H., Baumjohan, W., Paschmann, G., Lühr, H., and Sibeck, D. G. (1990). Upstream pressure variations associated with the bow shock and their effects on the magnetosphere. *J. Geophys. Res.: Space Phys.*, *95*(A4), 3773–3786. https://doi.org/10.1029/JA095iA04p03773

Formisano, V., Domingo, V., and Wenzel, K. P. (1979). The three-dimensional shape of the magnetopause. *Planet. Space Sci.*, *27*(9), 1137–1149. https://doi.org/10.1016/0032-0633(79)90134-X

García, K. S., and Hughes, W. J. (2007). Finding the Lyon-Fedder-Mobarry magnetopause: A statistical perspective. *J. Geophys. Res.: Space Phys.*, *112*(A6), A06229. https://doi.org/10.1029/2006JA012039

Gordeev, E., Sergeev, V., Honkonen, I., Kuznetsova, M., Rastätter, L., Palmroth, M., Janhunen, P., Tóth, G., Lyon, J., and Wiltberger, M. (2015). Assessing the performance of community-available global MHD models using key system parameters and empirical relationships. *Space Weather*, *13*(12), 868–884. https://doi.org/10.1002/2015SW001307

Grimmich, N., Plaschke, F., Archer, M. O., Heyner, D., Mieth, J. Z. D., Nakamura, R., and Sibeck, D. G. (2023). Study of extreme magnetopause distortions under varying solar wind conditions. *J. Geophys. Res.: Space Phys.*, *128*(8), e2023JA031603. https://doi.org/10.1029/2023JA031603

Grygorov, K., Šafránková, J., Němeček, Z., Pi, G., Přech, L., and Urbář, J. (2017). Shape of the equatorial magnetopause affected by the radial interplanetary magnetic field. *Planet. Space Sci.*, *148*, 28–34. https://doi.org/10.1016/j.pss.2017.09.011

Lin, R. L., Zhang, X. X., Liu, S. Q., Wang, Y. L., and Gong, J. C. (2010). A three-dimensional asymmetric magnetopause model. *J. Geophys. Res.: Space Phys.*, *115*(A4), A04207. https://doi.org/10.1029/2009JA014235

Liu, Z. Q., Lu, J. Y., Kabin, K., Yang, Y. F., Zhao, M. X., and Cao, X. (2012). Dipole tilt control of the magnetopause for southward IMF from global magnetohydrodynamic simulations. *J. Geophys. Res.: Space Phys.*, *117*(A7), A07207. https://doi.org/10.1029/2011JA017441

Liu, Z. Q., Lu, J. Y., Wang, C., Kabin, K., Zhao, J. S., Wang, M., Han, J. P., Wang, J. Y., and Zhao, M. X. (2015). A three-dimensional high Mach number asymmetric magnetopause model from global MHD simulation. *J. Geophys. Res.: Space Phys.*, *120*(7), 5645–5666. https://doi.org/10.1002/2014JA020961

Lu, J. Y., Liu, Z. Q., Kabin, K., Zhao, M. X., Liu, D. D., Zhou, Q., and Xiao, Y. (2011). Three dimensional shape of the magnetopause: Global MHD results. *J. Geophys. Res.: Space Phys.*, *116*(A9), A09237. https://doi.org/10.1029/2010JA016418

Maezawa, K., and Hori, T. (1998). The distant magnetotail: Its structure, IMF dependence, and thermal properties. In A. Nishida, et al. (Eds.), *New Perspectives on the Earth's Magnetotail* (pp. 1–19). Washington, DC: American Geophysical Union. https://doi.org/10.1029/GM105p0001

McFadden, J. P., Carlson, C. W., Larson, D., Ludlam, M., Abiad, R., Elliott, B., Turin, P., Marckwordt, M., and Angelopoulos, V. (2008). The THEMIS ESA plasma instrument and in-flight calibration. *Space Sci. Rev.*, *141*(1), 277–302. https://doi.org/10.1007/s11214-008-9440-2

Nguyen, G., Aunai, N., de Welle, B. M., Jeandet, A., Lavraud, B., and Fontaine, D. (2022). Massive multi-mission statistical study and analytical modeling of the Earth's magnetopause: 3. An asymmetric non indented magnetopause analytical model. *J. Geophys. Res.: Space Phys.*, *127*(1), e2021JA030112. https:

//doi.org/10.1029/2021JA030112

Palmroth, M., Janhunen, P., Pulkkinen, T. I., and Peterson, W. K. (2001). Cusp and magnetopause locations in global MHD simulation. *J. Geophys. Res.: Space Phys.*, *106*(A12), 29435–29450. https://doi.org/10.1029/2001JA900132

Petrinec, S. M., and Russell, C. T. (1996). Near-Earth magnetotail shape and size as determined from the magnetopause flaring angle. *J. Geophys. Res.: Space Phys.*, *101*(A1), 137–152. https://doi.org/10.1029/95JA02834

Šafránková, J., Dušík, Š., and Němeček, Z. (2005). The shape and location of the high-latitude magnetopause. *Adv. Space Res.*, *36*(10), 1934–1939. https://doi.org/10.1016/j.asr.2004.05.009

Samsonov, A. A., Němeček, Z., Šafránková, J., and Jelínek, K. (2012). Why does the subsolar magnetopause move sunward for radial interplanetary magnetic field?. *J. Geophys. Res.: Space Phys.*, *117*(A5), A05221. https://doi.org/10.1029/2011JA017429

Samsonov, A. A., Gordeev, E., Tsyganenko, N. A., Šafránková, J., Němeček, Z., Šimůnek, J., Sibeck, D. G., Tóth, G., Merkin, V. G., and Raeder, J. (2016). Do we know the actual magnetopause position for typical solar wind conditions?. *J. Geophys. Res.: Space Phys.*, *121*(7), 6493–6508. https://doi.org/10.1002/2016JA022471

Shue, J. H., Chao, J. K., Fu, H. C., Russell, C. T., Song, P., Khurana, K. K., and Singer, H. J. (1997). A new functional form to study the solar wind control of the magnetopause size and shape. *J. Geophys. Res.: Space Phys.*, *102*(A5), 9497–9511. https://doi.org/10.1029/97JA00196

Shue, J. H., Song, P., Russell, C. T., Steinberg, J. T., Chao, J. K., Zastenker, G., Vaisberg, O. L., Kokubun, S., Singer, H. J., … Kawano, H. (1998). Magnetopause location under extreme solar wind conditions. *J. Geophys. Res.: Space Phys.*, *103*(A8), 17691–17700. https://doi.org/10.1029/98JA01103

Sibeck, D. G., Siscoe, G. L., Slavin, J. A., and Lepping, R. P. (1986). Major flattening of the distant geomagnetic tail. *J. Geophys. Res.: Space Phys.*, *91*(A4), 4223–4237. https://doi.org/10.1029/JA091iA04p04223

Suvorova, A. V., Shue, J. H., Dmitriev, A. V., Sibeck, D. G., McFadden, J. P., Hasegawa, H., Ackerson, K., Jelínek, K., Šafránková, J., and Němeček, Z. (2010). Magnetopause expansions for quasi-radial interplanetary magnetic field: THEMIS and Geotail observations. *J. Geophys. Res.: Space Phys.*, *115*(A10), A10216. https://doi.org/10.1029/2010JA015404

Suvorova, A. V., and Dmitriev, A. V. (2015). Magnetopause inflation under radial IMF: Comparison of models. *Earth Space Sci.*, *2*(4), 107–114. https://doi.org/10.1002/2014EA000084

Tátrallyay, M., Erdös, G., Németh, Z., Verigin, M. I., and Vennerstrom, S. (2012). Multispacecraft observations of the terrestrial bow shock and magnetopause during extreme solar wind disturbances. *Ann. Geophys.*, *30*(12), 1675–1692. https://doi.org/10.5194/angeo-30-1675-2012